Applied Catalysis B: Environmental 343 (2024) 123536

Contents lists available at ScienceDirect

Applied Catalysis B: Environmental

journal homepage: www.elsevier.com/locate/apcatb

Bifunctional catalyst with high efficiency for converting hydrocarbons: The enhanced diffusion between micro and meso-pores

Zhengkai Cao [a,b,*], Sijia Ding [a], Rong Guo [a], Zhentao Chen [b], Jiahuan Yu [b], Ziming Wu [a], Daowei Gao [c,**], Aijun Duan [b], Hanbang Liu [a], Xia Zhang [a,**]

[a] Dalian Research Institute of Petroleum and Petrochemicals, SINOPEC, Dalian 116041, Liaoning, China
[b] State Key Laboratory of Heavy Oil Processing, China University of Petroleum, Beijing 102249, China
[c] School of Chemistry and Chemical Engineering, University of Jinan, Jinan 250022, China

ARTICLE INFO

Keywords:
Hydrocracking
Catalysts
Diffusivity
Activity
Selectivity

ABSTRACT

The influences of the distance between the hydrogenation center and cracking center and diffusivities of catalysts on hydrocracking behaviors were investigated. It was initially found that, compared with the catalysts with only micromeso-Y zeolite or meso-Al_2O_3, the diffusivities of combined catalysts with both Y zeolite and Al_2O_3 could be significantly improved. The NiW/Y-A catalyst presents the best diffusivity due to the introduction of pure meso-Al_2O_3. The property of active metals and acidity play an important role on the adsorption ability of catalyst. The n-dodecane hydrocracking results showed that the NiW/Y-A catalyst with the lowest dispersion degree of metals, acidity and proportion of active WS_2 phase presented the highest activity due to its superior diffusivity. The results also revealed that a closer distance between the hydrogenation and cracking centers leads to a higher selectivity of iso-cracking, liquid yield and better stability of catalysts. The above findings provide a potential novel method for designing catalysts with high activities and selectivities.

1. Introduction

Bifunctional catalysts with metal-acid sites for the converting hydrocarbons into fuels and chemical materials have been widely investigated [1–4]. Zeolites with regular structure of micropores are generally applied as the supports for bifunctional hydrocracking catalysts [5–8]. As the kinetic diameter of a molecule reaches the pore size of a zeolite, the poor diffusivity will decrease the activity and limit its application [5]. The deficiency of microzeolite in terms of diffusion can be overcome by introducing mesopores, which can improve the pore accessibility and reactant transport [6,7]. Shao et al. found that anion transfer over a microwater/1,2-dichloroethane interface could be enhanced by β-octafluoro-meso-octamethylcalixpyrrole [8]. Krishna et al. provided a convenient method to describe mixture diffusion in micro- and mesoporous materials on the basis of accessible pore volume inside the porous structures [9]. Malekian et al. applied a zero-length column method to evaluate the diffusion path in zeolite. The results showed that the ZSM-5 with mesopores presented higher diffusion time constants [10]. Li et al. obtained supercapacitors with high energy and power by adjusting the ratio of micro- and mesopores for biomass-derived ultrathin carbon sheets; this improvement could be explained by fast mass-transport channels, resulting in high power density [11].

As for bifunctional hydrocracking catalysts, both the diffusion of pores in support and the diffusivity between metal and acid sites determine the activity and selectivity [12–16]. Weisz et al. proposed the maximum distance between metal sites and acid sites, exceed which catalytic activity will decrease [12]. Zečević et al. prepared two kinds of catalysts, including Pt-Y/A and Pt-Y/A. For Pt-Y/A catalyst, the Pt metal was loaded on the zeolite, in which the Pt particles were closely located with acid sites. For Pt-A/Y catalyst, the Pt metal was loaded on Al_2O_3 support, in which Pt particles were within a nanoscale distance between acid sites and metal sites. From the results of hydrocracking n-C10 and n-C19, the isomerization reaction could be enhanced by the nano-distance between the acid sites and metal sites [13]. However, Bouchy et al. proposed that there are no obvious relationship between isomerization selectivity and distance of acid sites and metals sites [14]. de Jong et al. compared the influence of the distance of metal sites and acid sites in bifunctional catalysts with different zeolites [15]. The

* Corresponding author at: Dalian Research Institute of Petroleum and Petrochemicals, SINOPEC, Dalian 116041, Liaoning, China.
** Corresponding authors.
E-mail addresses: xiaocao19910926@163.com (Z. Cao), chm_gaodw@ujn.edu.cn (D. Gao), zhangxia.fshy@sinopec.com (X. Zhang).

https://doi.org/10.1016/j.apcatb.2023.123536
Received 6 August 2023; Received in revised form 13 November 2023; Accepted 16 November 2023
Available online 21 November 2023
0926-3373/© 2023 Elsevier B.V. All rights reserved.

results showed that, for ZSM-5 containing catalysts, more mono-branched isomers would be generated, which was not affected by the distance between metal sites and active sites from closest to microscale. For hydrocracking catalysts with Beta or Y zeolite, the activity and selectivity can be improved from the nanoscale distance between metal sites and acid sites. The authors assigned the difference to the high diffusional barriers of branched isomers within ZSM-5 micropores. Wang et al. investigated the effect of different distances between metal and acid sites of bifunctional catalysts on the hydrocracking behaviors of long chain alkanes [16]. It demonstrated that the diffusivity and the accessibility of Pt directly influence the isomerization selectivity of long-chain alkanes.

Above all, the effects of diffusivity and distance between acid and metal sites for bifunctional catalysts with noble metals on hydrocracking reactions have been investigated by some researchers. However, the influences on industrial hydrocracking catalysts with normal metals, including Ni, W, Mo and Co have not been reported yet. The conventional zeolites in industrial hydrocracking catalysts include Y, ZSM-5, Beta and SAPO zeolites [17–20]. Y zeolite with a strong ability to convert hydrocarbons in fossil fuel is the most widely applied support for hydrocracking catalysts [5]. Meanwhile, mesoporous alumina with high hydrothermal stability and mechanical strength but low price was selected as the support for industrial hydrotreating catalysts. Therefore, Y zeolite with micro- and mesopores was chosen as the acidic support for cracking hydrocarbons, and mesoporous alumina was selected for mixing with Y zeolite to further improve its diffusivity. Moreover, the normal Ni and W active metals were chosen to load on the supports of hydrocracking catalysts in this study.

Some novel methods have been reported to prepare bifunctional catalysts with varying distances between metal sites and acid sites [21, 22]. Physically mixed a catalyst with metals and zeolite is a conventional approach to adjust the distance between metal and acid sites from micron to millimeter scale [23]. In our study, we prepared different hydrocracking catalysts containing micromeso-Y zeolite and mesoporous alumina. The nickel and tungsten metals loading on Y zeolite and then mixed with alumina (A) was referred as NiW/Y-A. The nickel and tungsten metals loading on alumina (A) and then mixed with Y zeolite was referred as NiW/A-Y. The nickel and tungsten metals loading on the mixture of alumina (A) and Y zeolite was referred as NiW/AY. The hydrocracking behaviors of n-dodecane were compared with those of NiW/Al_2O_3 and NiW/Y catalysts. Finally, the effects of the distance between the hydrogenation center and cracking center and the diffusion of the reactant on the hydrocracking performance were disclosed. A bifunctional catalyst with high activity was obtained by establishing a micro- and meso-support system.

2. Experimental

2.1. Catalyst preparation

The bifunctional hydrocracking catalysts were synthesized by the following methods. Nickel nitrate hexahydrate ($Ni(NO_3)_2$•6 H_2O, CAS: 13478–00–7, Aladdin) ($(NH_4)_6H_2W_{12}O_{40}$·XH_2O, CAS: 12333–11–8, Aladdin) and ammonium metatungstate are selected as W and Ni sources, respectively. The above W and Ni sources are adequately dissolved in pure water by an ultrasonic apparatus. The pH of aqueous solution for ammonium metatungstate is 5.8, and the pH of aqueous solution for nickel nitrate hexahydrate is 5.4. The impregnation solutions are the same for all the catalysts. A stepwise equal volume impregnation method is applied to loading active metals. The W sources is impregnated on the powder initially. The contact time of powder with impregnation solutions is 6 h. After each impregnation, the powder will be dried at 60 °C and calcined at 450 °C for 6 h.

For the NiW/AY catalyst, the Ni and W active metals were loaded on the mixture of prepared micromeso-Y zeolite and Al_2O_3. For the NiW/A-Y catalyst, the Ni and W active metals were loaded on Al_2O_3 and then mixed with HY zeolite. For the NiW/Y-A catalyst, the Ni and W active metals were loaded on micromeso-Y zeolite and then mixed with Al_2O_3. The mass percentages of micromeso-Y zeolite in the support are fixed at 50% in the above three catalysts. Noticeably, the concentrations of NiO and WO_3 in all the catalysts were controlled at 3.0 m% and 12.0 m%, respectively. The mentioned NiW/Y and NiW/Al_2O_3 catalysts in the main text come from the NiW/Y-A and NiW/A-Y catalysts, respectively.

The Si/Al ratio in the above Y zeolite is 10. The pore properties of Y and Al_2O_3 are summarized in Table S1. The actual composition of different catalysts was detected by XRF analysis, and the results are shown in Table S2. The average particle sizes of NiW/A-Y, NiW/Y-A and NiW/AY catalysts obtained from SEM images are approximately 1.4 μm, 1.5 μm and 1.5 μm.

2.2. Catalyst characterization

The samples were characterized by various measurements, and the detailed methods for the above measurements are provided in the Supporting Information.

2.3. Calculation method

The calculation methods for the conversion of n-dodecane, hydrocracking rate constant *k*, turnover frequency (*TOF*), and capacity factor *K'* are provided in the Supporting Information.

2.4. Catalytic test

The n-dodecane hydrocracking performances over various catalysts were tested on a micro-scale unit. 1 g catalyst was filled in the middle of the reactor. The catalyst was sulfided by 2.0 v% CS_2 in cyclohexane solution. As the temperature of reactor reaches 180 °C, the sulfidation solution was introduced into reactor with a rate of 15 mL/h. After 2 h, the temperature was heat up to 230 °C and hold for 8 h. Thereafter, the temperature was increased to 360 °C and hold for 4 h. Finally, the sulfidation procedure was finished.

After sulfurization, the reactant of n-dodecane mixed with 1000 ppm CS_2 was pumped into the unit. The pressure and H_2/Oil ratio were fixed at 4 MPa and 100, respectively. The effect of weight time on the n-dodecane hydrocracking performances was studied for different catalysts. Weight time was defined as $t = \omega_{cat}/\eta_{feed}$. ω_{cat} represents the catalyst weight, and η_{feed} denotes the total molar number of feed introducing into the reactor [24]. Finally, liquid product was analyzed by a gas chromatography instrument.

The compositions of liquid product were analyzed by a multidimensional gas chromatography in PONA method. The chromatographic column: PONA column, 50 m × 0.2 mm × 0.5 μm; Vaporization chamber temperature: 230 ℃; Detector (FID) temperature: 230 ℃; Column temperature: initial temperature 35 ℃, maintain for 15 min, increase to 200 ℃ at 2 ℃/min, and maintain for 5 min; Carrier gas: N_2 with high purity; Pressure before column: 0.08 MPa; Injection volume: 0.4 μL; Split ratio: 100:1.

The conversion of reactant (*X*) was calculated by the following equation:

$$X = (1 - (1 - Y_g) * M_n) * 100\% \quad (1)$$

In which Y_g represents the yield of gas; M_n represents the contents of n-dodecane in liquid product.

The order of n-dodecane hydrocracking reaction was treated as pseudo-first. The hydrocracking rate constant k_n was calculated by the following equation:

$$k_n = \frac{f}{m} \ln\left(\frac{1}{1-\tau}\right) \quad (2)$$

Where *f* signified the feed rate for n-dodecane (mol/s), *m* signified the

mass of catalyst (g), and τ signified the conversion of n-dodecane [24].

3. Results and discussions

3.1. Properties of catalysts

The N_2 adsorption and desorption isotherms of different catalysts and pore distributions of different catalysts are shown in Fig. 1A and B, respectively. All the catalysts containing the Al_2O_3 support present H3-type hysteresis loops, and the NiW/Y catalyst shows H4-type hysteresis loops. In Fig. 1B, the NiW/Al_2O_3 catalyst presents a wide band at 2–50 nm and a peak at a pore width of 17.5 nm, confirming that Al_2O_3 is mainly mesoporous. The NiW/Y catalyst presents a band at 1.5–5.5 nm and a peak at a pore width of 4.5 nm, indicating that the Y zeolite contains micropores and mesopores. Meanwhile, the catalysts containing Y zeolites and Al_2O_3 show two peaks at pore widths of 4.5 nm and 17.5 nm.

The pore parameters of different catalysts calculated from Fig. 1A are summarized in Table 1. The NiW/Al_2O_3 catalyst presents an extremely higher mesoporous volume than microporous volume. The NiW/Y catalyst possesses a relatively balanced mesoporous volume and microporous volume. The surface area and pore size of the NiW/Y catalyst are the highest at 425.1 m^2/g and the lowest at 2.4 nm, respectively. Moreover, the NiW/Al_2O_3 catalyst possesses the largest pore size of 11.7 nm. The surface areas and pore sizes of the NiW/A-Y, NiW/Y-A and NiW/AY catalysts are similar. The NiW/Y-A catalyst exhibits a relatively lower V_{meso} than the other two catalysts. In addition, the ratios of V_{micro} and V_{meso} for the catalysts containing Y and Al_2O_3 supports follow the sequence of NiW/A-Y (0.20) < NiW/AY (0.23) < NiW/Y-A (0.28), indicating that the microporosity of NiW/Y-A is the highest.

The XRD patterns of different catalysts are shown in Fig. S1. The peaks a t 6.3°, 10.3°, 12.0°, 15.8°, 18.9°, 20.6°, 23.9°, 27.4° and 31.8° are ascribed to Y zeolites. The peak at 33.6 ° is assigned to WO_3 species (JCPDS 32–1395), which only appears in the XRD patterns of NiW/Y-A and NiW/Y catalysts. Two weak peaks at 45.9 ° and 66.9 ° (JCPDS 47–1292) assigned to γ-Al_2O_3 can be observed in the XRD patterns of NiW/Al_2O_3 catalyst. The XRD patterns of NiW/A-Y and NiW/AY catalysts exhibit obvious characteristic peaks of Y zeolite but no peaks of bulk WO_3 species. Therefore, alumina support with large pore size and pore volume can provide an excellent platform for active metals to load and disperse. Too much active metals loading on Y zeolite with micro and mesopores will lead to the agglomeration of active metals.

SEM imaging and EDX elemental mapping of the NiW/A-Y, NiW/Y-A and NiW/AY catalysts are shown in Fig. 2. Al_2O_3 only contains Al, but Y zeolite contains Si and Al. According to the above principle, the particles containing Al_2O_3 or Y zeolite are marked out and numbered 1 and 2, respectively. For the NiW/A-Y catalyst, the distance between micron-sized particles of 1-NiW/Al_2O_3 and 2-Y zeolite is on the micron scale. The 1-NiW/Al_2O_3 part can be considered a hydrogenation center, and the 2-Y zeolite part can be considered a cracking center. Therefore, the hydrogenation centers and cracking centers for NiW/A-Y are separated on a micron scale. The hydrogenation centers and cracking centers for NiW/Y-A and NiW/AY catalysts are much closer. For the NiW/Y-A catalyst, the distance between particles of 1-Al_2O_3 and 2-NiW/Y zeolite is also on the micron scale. The Al_2O_3 in the NiW/Y-A catalyst can only be treated as an inert carrier without activity. Moreover, the distribution of active metal (W) over the NiW/AY catalyst is more even than that over the other two catalysts.

Table 1
Pore parameters of different catalysts.

Samples	S, $m^2 \cdot g^{-1}$	V_{meso}, $cm^3 \cdot g^{-1}$	V_{micro}, $cm^3 \cdot g^{-1}$	V_{micro}/V_{meso}	D, nm
NiW/A-Y	424.8	0.54	0.11	0.20	5.5
NiW/Y-A	421.4	0.47	0.13	0.28	5.2
NiW/AY	421.3	0.51	0.12	0.23	5.6
NiW/ Al_2O_3	233.3	0.76	0.01	0.01	11.7
NiW/Y	425.1	0.08	0.17	2.13	2.4

To obtain the chemical state of the W oxide phases over different catalysts, UV–vis DRS spectra of the NiW/Y-A, NiW/A-Y and NiW/AY catalysts were obtained and are shown in Fig. 3A. The region of 200–400 nm is assigned to the adsorption bands caused by charge transfer transitions of W oxide species [25]. The tetrahedral WO_4 (Td) species shows an absorption region of 205–240 nm. Meanwhile, the band at 250–300 nm is assigned to octahedral (Oh) symmetry (WO_6) species. WO_3 species absorb bands ranging from 350 to 400 nm [26,27]. The NiW/A-Y and NiW/AY catalysts exhibit two obvious adsorption peaks at approximately 206 nm and 251 nm but no bands from 350 to 400 nm. The NiW/Y-A catalyst presents a strong adsorption band at 350–400 nm, confirming the presence of bulk WO_3 species and poor dispersion degree of metals, which is in accordance with the XRD result.

The band gap energy (*Eg*) can be estimated by plotting $a^{1/2}$ versus photon energy ($h\nu$) [28,29]. The higher the value of *Eg* is, the better the dispersion of active metals [30]. From Fig. 3B, the *Eg* values of different catalysts follow the order of NiW/Y-A (3.4 eV) < NiW/A-Y (3.9 eV) < NiW/AY (4.2 eV). Therefore, the dispersion degree of active metals for the NiW/AY catalyst is the best, and the dispersion degree of active metals for the NiW/Y-A catalyst is the worst.

CO-IR spectra of different catalysts reduced by hydrogen at 500 °C are shown in Fig. S2. The adsorption bands in the region of

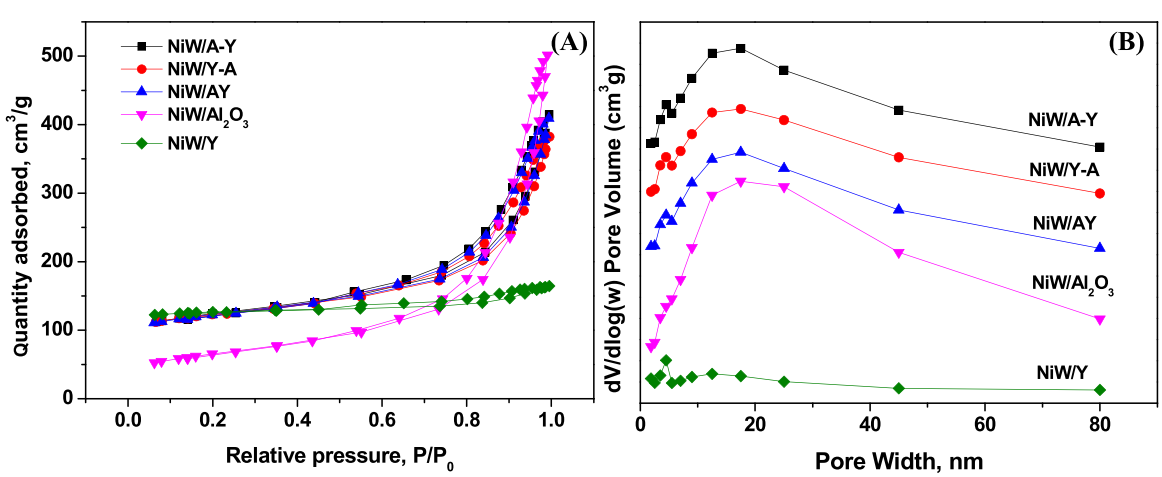

Fig. 1. N_2-adsorption and desorption isotherms of different catalysts (A); pore distributions of different catalysts (B).

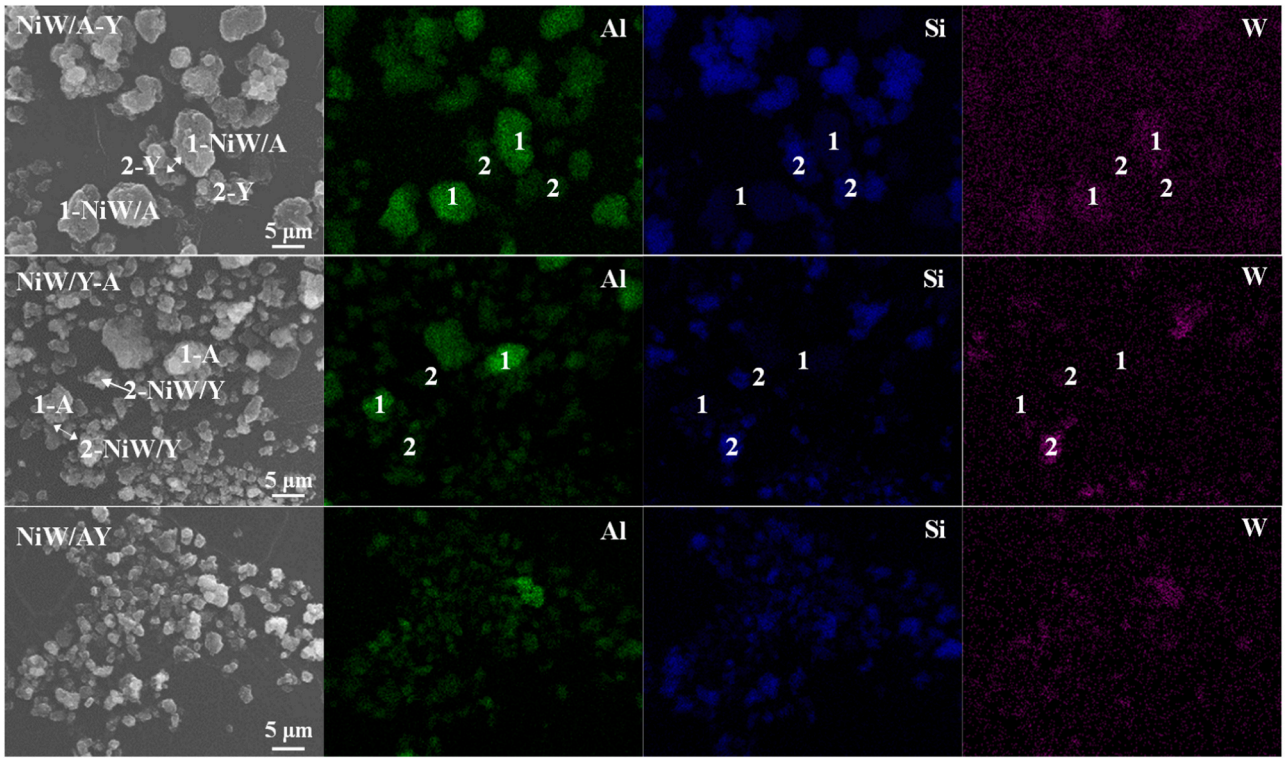

Fig. 2. SEM images and EDX-mapping (Al, Si and W) of different catalysts.

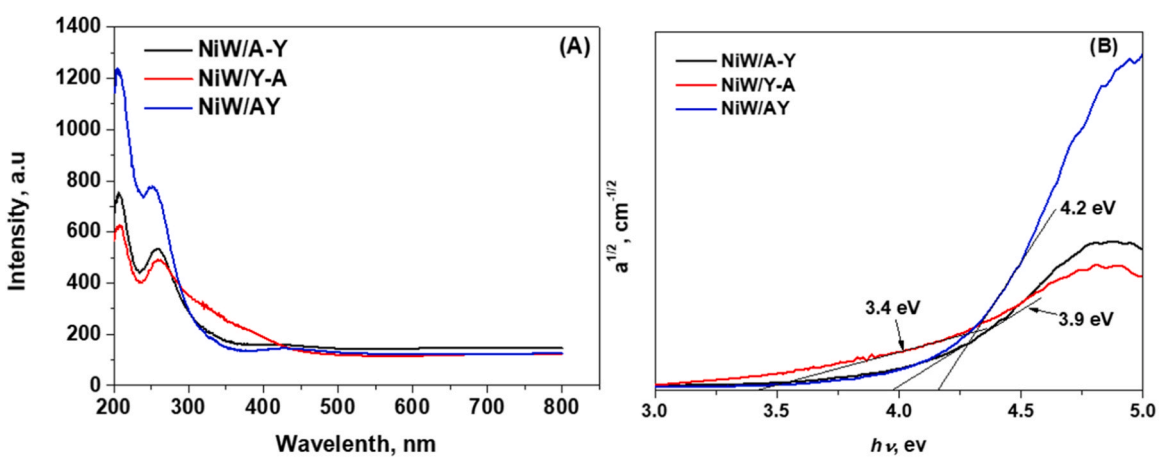

Fig. 3. UV–vis DRS spectra (A); plots of $a^{1/2}$ versus photon energy ($h\nu$) for different catalysts (B).

1900–2100 cm^{-1} are assigned to two states of CO adsorbed on reduced Ni sites. The bands appearing at 2050–2100 cm^{-1} (CO-linear adsorption) resulted from the Ni sites with lower reduction levels and better dispersion. The bands in the region of 2000–2050 cm^{-1} are indicative of moderately dispersed Ni^0 sties. Moreover, the bands below 2000 cm^{-1} (CO-bridged adsorption) demonstrate the existence of small clusters, which belong to poorly dispersed Ni species [31,32]. The bands at 2167 cm^{-1} and 2180 cm^{-1} are ascribed to the CO physically adsorbed on the supports of Y zeolite or/and Al_2O_3 [33]. The bands at about 2100 cm^{-1}, 2067 cm^{-1}, 2045 cm^{-1} and 2020 cm^{-1} appear in the CO-IR spectra of all the catalysts. The band at 2100 cm^{-1} indicates CO adsorbed on $Ni^{\delta+}$ species ($\delta = 1$ or 2) [33]. The band at 2067 cm^{-1} is attributed to nickel carbonyl species Ni^0 with better dispersion, whereas the bands at 2020 cm^{-1} and 2045 cm^{-1} suggest Ni species with a moderate dispersion degree [32]. There is no band appearing below 2000 cm^{-1}, suggesting that the dispersion degree of Ni species over all the catalysts is relatively high. The intensities of the bands assigned to CO adsorption on Ni species follow the order of NiW/Y-A < NiW/A-Y < NiW/AY. Therefore, the dispersion degree of Ni species for the NiW/AY catalyst is the best, which is in good agreement with the UV–vis DRS measurement.

H_2-TPD measurements were used to obtain the dispersion degrees of active metals over different catalysts, and the corresponding patterns are exhibited in Fig. S3. The first band from 60 °C to 400 °C results from H_2 adsorbed on the Ni atoms [34]. The second band from 500 °C to 800 °C is related to H_2 adsorbed on the Ni and W atoms [35]. The H_2 desorption amounts for various H_2-reduced catalysts are summarized in Table S3. The amounts of desorbed H_2 follow the order of NiW/Y-A (3.20 μmol/g) < NiW/A-Y (4.95 μmol/g) < NiW/AY (10.64 μmol/g). More desorbed H_2 will indicate a better dispersion degree of active metals. Therefore, the NiW/AY catalyst presents the best dispersion of active metals, and the dispersion of active metals for the NiW/Y-A catalyst is the worst. These results are consistent with the CO-IR and UV—vis DRS

measurements.

Raman spectroscopy was applied to investigate the surface crystalline phase of different catalysts, and the corresponding spectra are shown in Fig. 4. The bands in the region of 700–1200 cm^{-1} are ascribed to the vibration of W-O species [36]. The obvious peak at about 970 cm^{-1} is caused by the W═O symmetric stretching vibration mode of $W_7O_{24}^{6-}$ phases in the octahedral coordination W(Oh) [37]. The bands appearing at about 710 cm^{-1} and 810 cm^{-1} indicate the presence of WO_3 species [38]. The peak at about 835 cm^{-1} is assigned to the appearance of $W_6O_{19}^{2-}$ species. The absence of peaks assigned to bulk WO_3 phases indicates high dispersion degrees of NiW/AY and NiW/A-Y catalysts. The dispersion degree of active metals for the NiW/Y-A catalyst is poor due to the presence of WO_3 species, which is consistent with the XRD results.

H_2-TPR measurements were further carried out to obtain more characteristics of the loaded Ni and W species in the oxide and sulfide catalysts. The H_2-TPR profiles of oxide catalysts are shown in Fig. 5A. The NiW/A-Y and NiW/AY catalysts show two reduction peaks. The first peak at lower temperature is indicative of the reduction of octahedral W^{6+} species, W(Oh), and the second peak at higher temperature can be assigned to the reduction of W^{4+} species in tetrahedral coordination, W (Td) [39]. Generally, W(Oh) species can more easily sulfide and show high hydrogenation ability, and W(Td) species with a high dispersion degree are difficult to sulfide and present relatively low hydrogenation ability [26,40]. The first reduction peak at low temperature for the NiW/AY catalyst(473 °C) is lower than that of NiW/A-Y catalyst (487 °C). The second reduction peak at high temperature of NiW/AY catalyst (793 °C) is also lower than that of the NiW/A-Y catalyst (854 °C). The better reduction ability of the NiW/AY catalyst may be related to its better dispersion of active metals. In addition, the NiW/Y-A catalyst shows a sharp peak at approximately 650 °C assigned to the reduction of bulk WO_3 species [38].

The H_2-TPR profiles of different sulfide catalysts are shown in Fig. 5B. The sulfide NiW/A-Y and NiW/AY catalysts show one characteristic peak at low reduction temperatures. However, the NiW/AY catalyst shows two reduction peaks at low and high temperatures. The first peak at low temperature from 300° to 400°C should be related to the reduction of WS_2 or NiWS species that are weakly bonded to the catalyst surface [41]. The reduction temperature of the first peak for NiW/AY catalyst is the lowest among all the catalysts, which is consistent with H_2-TPR results of oxide catalysts. Meanwhile, the second reduction peak at about 610 °C for NiW/Y-A should be caused by the hydrogenation of sulfur in the bulk parts of WS_2-1ike sulfides [42]. It has been reported that the area of the low temperature peak allows for the determination of the number of active sites [41,42]. Accordingly, the concentration of active sites is the highest for NiW/AY catalyst, which is in accordance with CO-IR results.

Py-IR spectroscopy was carried out to determine the acid types and amounts of different catalysts. The Py-IR spectra recorded at 200 °C and 350 °C are shown in Fig. 6A and B. The band at 1490 cm^{-1} is indicative of Brönsted (B) and Lewis (L) acid sites. The band at approximately 1540 cm^{-1} corresponds to the B acid sites. The bands at 1450 cm^{-1} and 1610 cm^{-1} result from L acid sites [43]. The amounts of B and L acid sites obtained from Py-IR spectra for different catalysts are summarized in Table 2. The amounts of B acid sites follow the order of NiW/A-Y > NiW/AY > NiW/Y-A. Moreover, there is only L acid sites existed in NiW/Al_2O_3 catalyst. The B/L value for the NiW/Y-A catalyst is much lower than that of the other two catalysts. Therefore, loading more active metals on Y zeolite will causes more coverage of B acid sites. The NH_3-TPD spectra and total acidities of different catalysts are shown in Fig. S4 and Table S4, respectively. It shows that the total acidities follow the order of NiW/A-Y (0.94 mmol/g) > NiW/AY (0.91 mmol/g) > NiW/Y-A (0.82 mmol/g). The above results confirm that the acidities of NiW/Y-A is the lowest among the three catalysts, which is similar with the Py-IR result.

The ZLC measurement for detecting diffusion rate in crystals or particles was developed by Eic and Ruthven [44]. The differential bed of samples is initially saturated through adsorbable mediums. At time zero, the flowing adsorbable medium is replaced by a carrier fluid sufficiently, and then a desorption curve of adsorbate concentration over time can be obtained. ZLC instrument was applied to obtain the diffusivities of different catalysts. The desorption curves were detected at different temperatures using benzene solution, which were shown in Fig. 7. L represents the ZLC parameter. D/R^2 represents the apparent effective diffusivities. The L, De/R^2 and diffusion activation energies (Ea) in the hindered diffusion region of desorption curves are concluded in Table 3. The D/R^2 values at the temperatures higher than 80 °C for the five catalysts follow the order of NiW/Y-A > NiW/AY > NiW/A-Y > NiW/Al_2O_3 > NiW/Y. Therefore, it can be deduced that NiW/Y-A presents the best effective diffusivity. It should be noteworthy that NiW/Al_2O_3 catalyst with the largest pore but lower diffusivity than NiW/A-Y, NiW/Y-A and NiW/AY catalysts. It can suggest that introducing meso-Al_2O_3 can significantly improve the diffusivities of the combined catalysts. These results are very interesting and unconventional. To eliminate the influence of probe molecular and confirm the above results, the ZLC results detected by large probe molecular of 1,3, 5-trimethylbenzene over different catalysts and Al_2O_3 are shown in Fig. S5 and Table S5. It shows that the D/R^2 values follow a similar order of NiW/Y-A > NiW/AY > NiW/A-Y > NiW/Al_2O_3, which can confirm that the best diffusivity of NiW/Y-A among all the catalysts. Noticeably, the D/R^2 values at different temperatures of NiW/Al_2O_3 are significantly lower than those of pure meso-Al_2O_3, indicating that the diffusivity of Al_2O_3 support will be declined severely after loading active metals. Accordingly, the best diffusivity of NiW/Y-A catalyst can be related to the introduction of pure meso-Al_2O_3 with large pore and fast diffusivity.

Because the ZLC method can be used to obtain information on surface desorption and pore diffusion, the diffusional time constant also includes the effect of these two processes. The capacity factor K' is generally applied to represent the influence of surface desorption. A lower K' value will indicate a better desorption ability of catalyst [45]. K' calculated by L and D/R^2 obtained from different regions of desorption curves are concluded in Table 3. The K' values decrease with increasing temperature, indicating that a high temperature will decrease the surface desorption resistance. The K' values at temperatures higher than 80 °C follow the order of NiW/Y-A < NiW/AY < NiW/Al_2O_3 < NiW/A-Y < NiW/Y. Therefore, it can be deduced that the surface desorption of the reactant for the NiW/Y-A catalyst is fast, suggesting a better external diffusion performance between particles.

The reasons for this phenomenon must be discussed in depth. The capacity factor K' can be determined by adsorbate-adsorbent interactions. The adsorbent can adsorb on active metals and acid sites of the catalysts [46–49]. As reported, strong acidity and high total acid concentration can facilitate the adsorption of probe molecular [46,47]. Meanwhile, small particle size of active metals with high Gibbs free

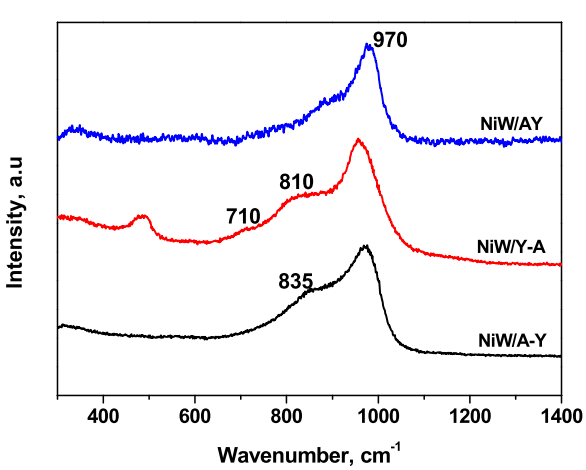

Fig. 4. Raman spectra of different catalysts.

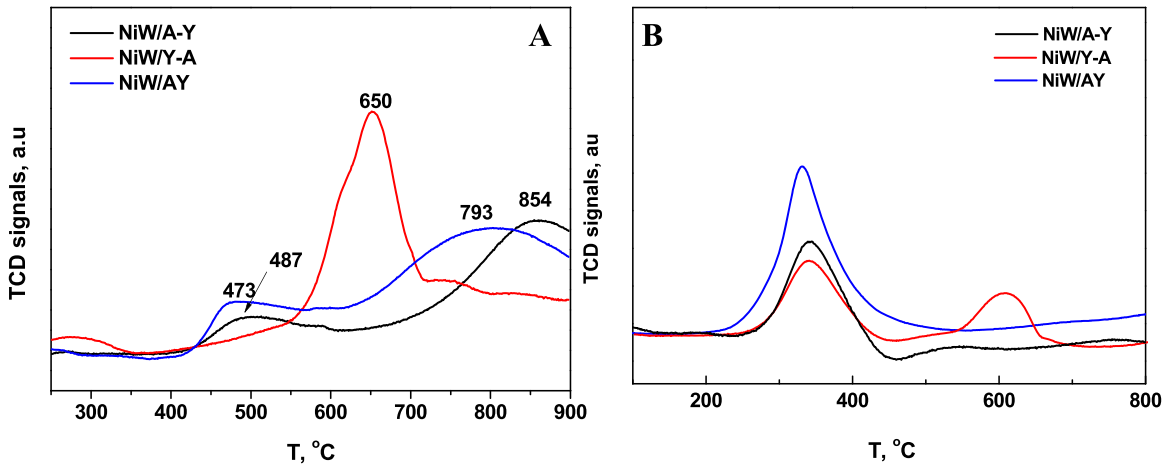

Fig. 5. H_2-TPR profiles of different oxide catalysts (A) and sulfide catalysts (B).

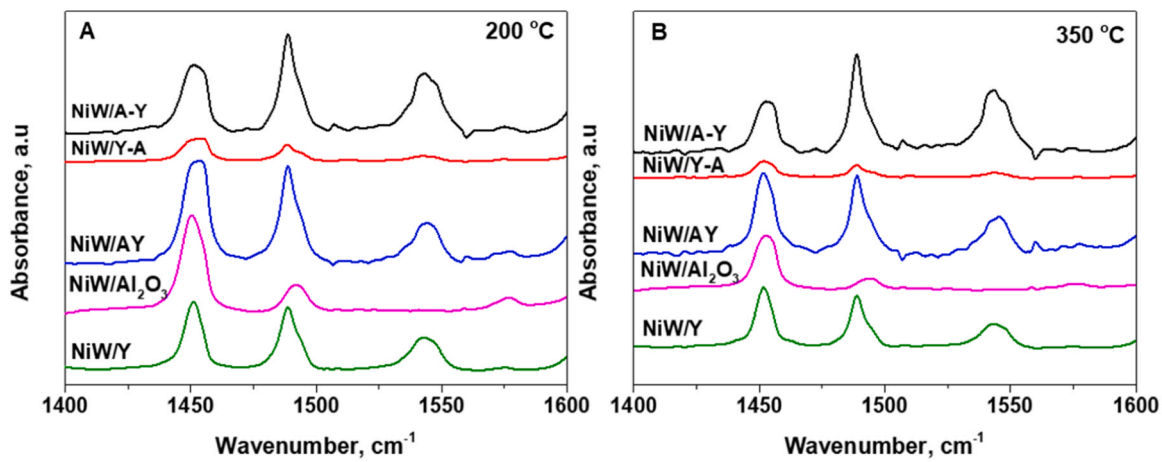

Fig. 6. Py-IR spectra of different catalysts desorbed at 200 °C (A) and 350 °C (B).

Table 2
the acidic properties of different catalysts, as determined by Py-IR spectra.

Catalysts	Acid amount (200 °C)/mmol·g^{-1}				Acid amount (350 °C)/mmol·g^{-1}			
	B	L	B+L	B/L	B	L	B+L	B/L
NiW/A-Y	0.039	0.031	0.070	1.26	0.037	0.022	0.059	1.68
NiW/Y-A	0.004	0.017	0.021	0.24	0.002	0.006	0.008	0.33
NiW/AY	0.030	0.049	0.079	0.61	0.021	0.030	0.051	0.70
NiW/Al_2O_3	0	0.044	0.044	0	0	0.023	0.023	0
NiW/Y	0.018	0.027	0.045	0.67	0.015	0.020	0.035	0.75

energy changes (ΔG) will present strong adsorption ability [50,51]. Among the NiW/A-Y, NiW/Y-A and NiW/AY catalysts, NiW/Y-A catalyst with the weakest acidity (Py-IR), largest particle size and worst dispersion of active metals (Uv-vis DRS) will exhibit the weakest adsorption strength between adsorbate and adsorbent. The weakest adsorption strength of NiW/Y-A catalyst will allow the lowest *K'* value and the best desorption ability. The corresponding principle for the best diffusivity of NiW/Y-A catalyst is shown in Scheme 1.

In addition, the relatively high *K'* value of NiW/A-Y catalyst should be related to its strongest acidity among the three combined catalysts. The highest *K'* values of NiW/Y catalyst should be related to fact that the amount of active metals with strong adsorption ability in the detected sample is twice as much as NiW/A-Y, NiW/Y-A and NiW/AY catalysts.

The CO-IR spectra of sulfide catalysts are presented in Fig. 8. The peaks at about 2070 cm^{-1}, 2133 cm^{-1} and 2159 cm^{-1} are assigned to the CO adsorption of S-edges in WS_2 phase, WO_xS_y and surface OH (Sur-OH) group, respectively [52–54]. The proportions of different species over sulfide catalysts are concluded in Table 4. It can be clearly seen that proportion of S-edges in WS_2 phases follow the order of NiW/Y-A < NiW/A-Y < NiW/AY. Meanwhile, the intensity of CO adsorbed on Sur-OH group follow the order of NiW/Y-A > NiW/A-Y > NiW/AY. A high proportion of WS_2 phases and low proportion of Sur-OH group will indicate a good dispersion degree of active metals [54]. Therefore, the dispersion degree and concentration of WS_2 species will follow the order of NiW/Y-A < NiW/A-Y < NiW/AY.

XPS measurements were applied to obtain the distributions of W species over the surface of different sulfide catalysts, and the corresponding spectra are shown in Fig. 9. As reported, the binding energies for W^{4+} (WS_2) are approximately 32.2 eV and 34.3 eV. The binding energies for W^{5+} are 32.9 eV and 34.8 eV. The binding energies for W^{6+}

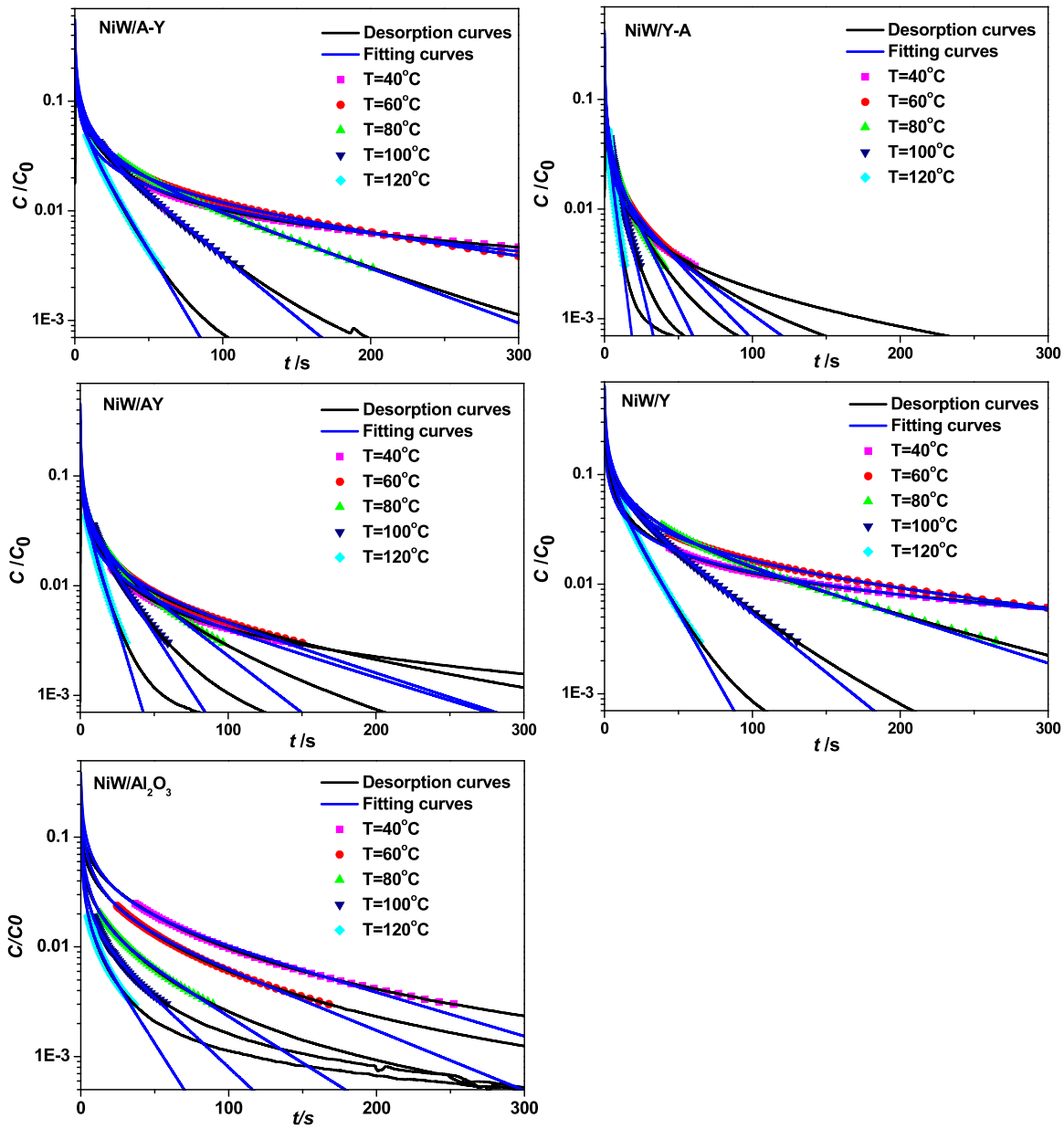

Fig. 7. ZLC desorption curves of different oxide catalysts. (Absorbent: benzene solution).

species are 36.0 eV and 38.1 eV [26,55]. The peak-fitting data for different catalysts are summarized in Table 5. The proportions of W^{4+} species follow the order of NiW/AY (0.30) > NiW/A-Y-25 (0.20) > NiW/Y-A (0.16). The NiW/AY catalyst shows the highest proportion of W^{4+} species, which is consistent with the CO-IR spectra of different sulfide catalysts. The highest proportion of W^{4+} species for NiW/AY catalyst can be related to its highest dispersion degree of active metals. In addition, the W^{4+} species is generally considered the active phase with high hydrogenation ability [55]. It can be deduced that the hydrogenation ability of the NiW/AY catalyst is the best among the above three catalysts.

The HETEM images of different catalysts are presented in Fig. S6. The layers and length distributions of WS_2 slabs for different catalysts are shown in Fig. 10A and B, respectively. All the catalysts exhibit more WS_2 slabs with 1 and 2 layers and lengths in the region of 2–4 nm. The properties of the WS_2 slabs are summarized in Table 5. The average length of WS_2 slabs ($\overline{L}$) follows the order of NiW/Y-A (3.6 nm) > NiW/A-Y (3.3 nm) > NiW/AY (3.0 nm). The dispersion degrees of WS_2 slabs (f_W) follow the order of NiW/AY (0.24) > NiW/A-Y (0.22) > NiW/Y-A (0.20). The sulfide NiW/AY catalyst presents a relatively better dispersion of active WS_2 phases.

ZLC measurement is also applied to confirm the diffusivities of different evaluated sulfide catalysts. The desorption curves of sulfide NiW/A-Y, NiW/Y-A and NiW/AY catalysts adsorbed by 1,3,5-trimethylbenzene are shown in Fig. S7, and the corresponding De/R^2 values are concluded in Table S6. It can be seen that the De/R^2 values at all temperatures follow the order of NiW/Y-A > NiW/AY > NiW/A-Y, which is similar with that of oxide catalysts. All the sulfide catalysts exhibits relatively lower De/R2 values than the corresponding oxide catalysts. The best diffusivity of sulfide NiW/Y-A catalyst can be related to the introduction of pure Al_2O_3 support. Accordingly, loading certain amounts of active metals on Al_2O_3 support will significantly decrease the diffusivity for oxide and sulfide catalysts.

Table 3
Analysis results of the desorption curves for different oxide catalysts. (Absorbent: benzene solution).

T, °C	L	D/R^2, 1/s	*K'*	*Ea*, KJ/mol
NiW/A-Y				
40	228.15	$2.76 * 10^{-4}$	447.3	
60	140.33	$4.55 * 10^{-4}$	441.2	
80	68.75	$1.20 * 10^{-3}$	341.4	
100	41.69	$2.71 * 10^{-3}$	249.3	
120	34.28	$5.63 * 10^{-3}$	146.0	39.8
NiW/Y-A				
40	197.56	$2.22 * 10^{-3}$	65.1	
60	123.34	$3.62 * 10^{-3}$	64.0	
80	64.25	$6.66 * 10^{-3}$	66.8	
100	36.85	$1.42 * 10^{-2}$	54.6	
120	28.87	$2.72 * 10^{-2}$	36.4	28.0
NiW/AY				
40	204.85	$8.39 * 10^{-4}$	155.2	
60	165.85	$1.04 * 10^{-3}$	154.6	
80	81.46	$2.48 * 10^{-3}$	132.0	
100	50.19	$5.06 * 10^{-3}$	105.0	
120	37.06	$1.10 * 10^{-2}$	65.4	32.4
NiW/Al_2O_3				
40	84.11	$9.52 * 10^{-4}$	312.2	
60	93.76	$1.31 * 10^{-3}$	203.5	
80	124.08	$2.00 * 10^{-3}$	100.7	
100	137.53	$2.99 * 10^{-3}$	60.8	
120	133.32	$5.02 * 10^{-3}$	37.4	21.0
NiW/Y				
40	267.95	$1.63 * 10^{-4}$	663.7	
60	121.61	$3.62 * 10^{-4}$	658.4	
80	55.09	$1.04 * 10^{-3}$	505.9	
100	31.16	$2.69 * 10^{-3}$	345.8	
120	23.8	$4.06 * 10^{-3}$	300.0	47.2

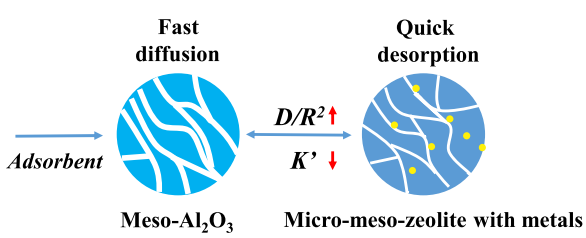

Scheme 1. Principle for the best diffusivity of NiW/Y-A catalyst.

3.2. Catalytic performance

The n-dodecane hydrocracking performances evaluated at various weight times (τ) over different catalysts are shown in Fig. 11A. The temperature, pressure and volume ratio of hydrogen and oil are fixed at 320 °C, 4 MPa and 100, respectively. The NiW/Al_2O_3 catalyst presents conversions lower than 1% to crack n-dodecane at different weight times. Therefore, the cracking activities of the NiW/Al_2O_3 or Al_2O_3 parts in the combined catalysts of NiW/A-Y, NiW/Y-A and NiW/AY can also be neglected. Noticeably, the NiW/Y-A catalyst shows a higher conversion of cracking n-dodecane than the NiW/A-Y and NiW/AY catalysts, even though it possesses a low pore size and pore volume, poor dispersion of active metals and weak acidities; this can be attributed to the fact that the NiW/Y-A catalyst possesses the best diffusivity. It should be noted that the NiW/Y-A, NiW/A-Y and NiW/AY catalysts present higher n-dodecane hydrocracking activities than the NiW/Y catalyst, due to their better diffusivities. Therefore, diffusivity plays an important role in the activity of hydrocracking catalysts.

Table 4
the proportions of different species over sulfide catalysts determined by CO-IR.

Catalysts	S-edge in WS_2, %	WO_xS_y, %	Surface OH, %
NiW/A-Y	71.2	6.2	22.7
NiW/Y-A	64.1	9.9	26.0
NiW/AY	84.5	2.1	13.5

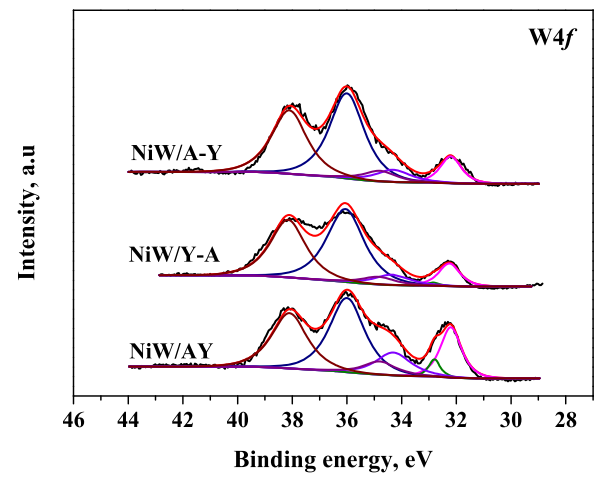

Fig. 9. XPS spectra of different sulfided catalysts.

Table 5
the properties of WS_2 species for different catalysts.

Catalysts	distribution of W species, %			WS_2 morphology parameter		
	W^{4+}	W^{5+}	W^{6+}	$\overline{L}$, nm	$\overline{N}$	f_W
NiW/A-Y	0.20	0.05	0.75	3.3	1.8	0.22
NiW/Y-A	0.16	0.05	0.79	3.6	1.9	0.20
NiW/AY	0.28	0.09	0.63	3.0	1.6	0.24

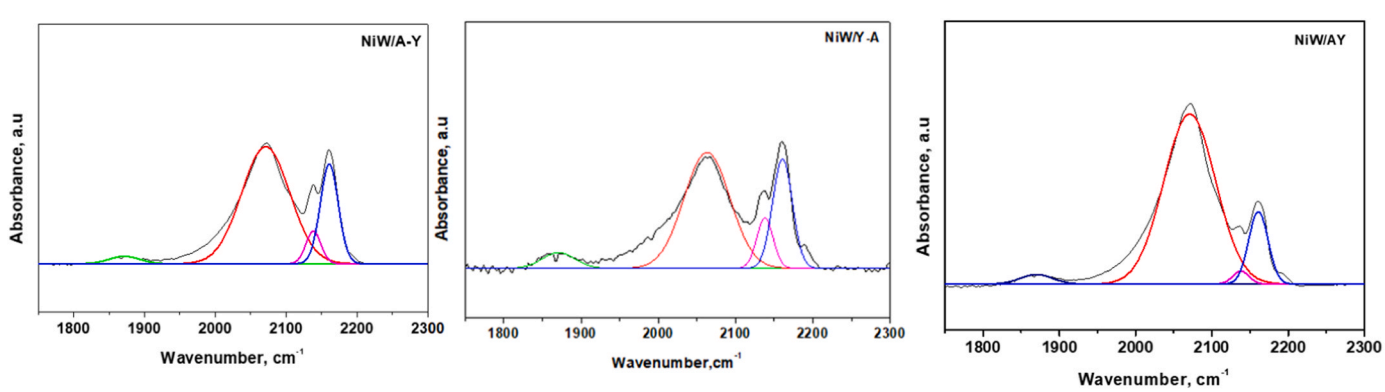

Fig. 8. the CO-IR spectra of different sulfide catalysts.

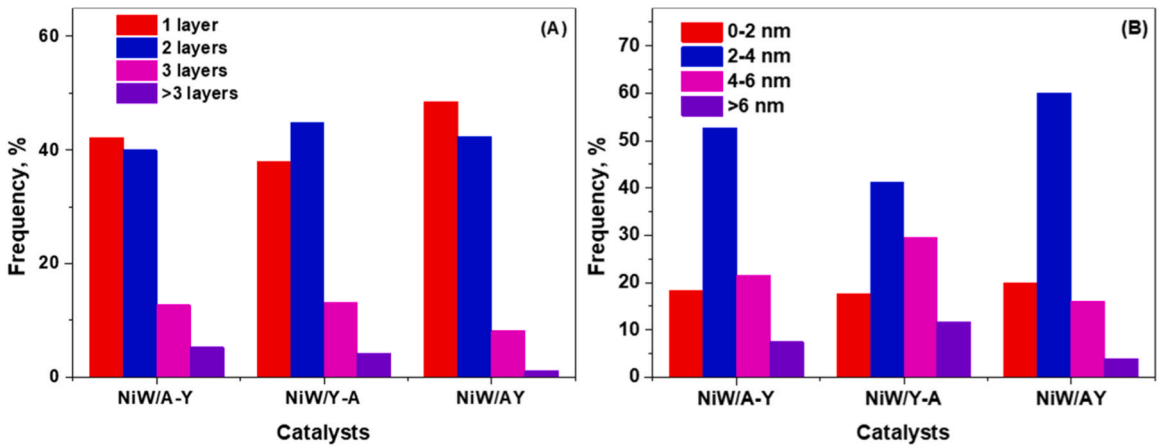

Fig. 10. Layers (A) and lengths (B) distributions of WS_2 slabs for different catalysts.

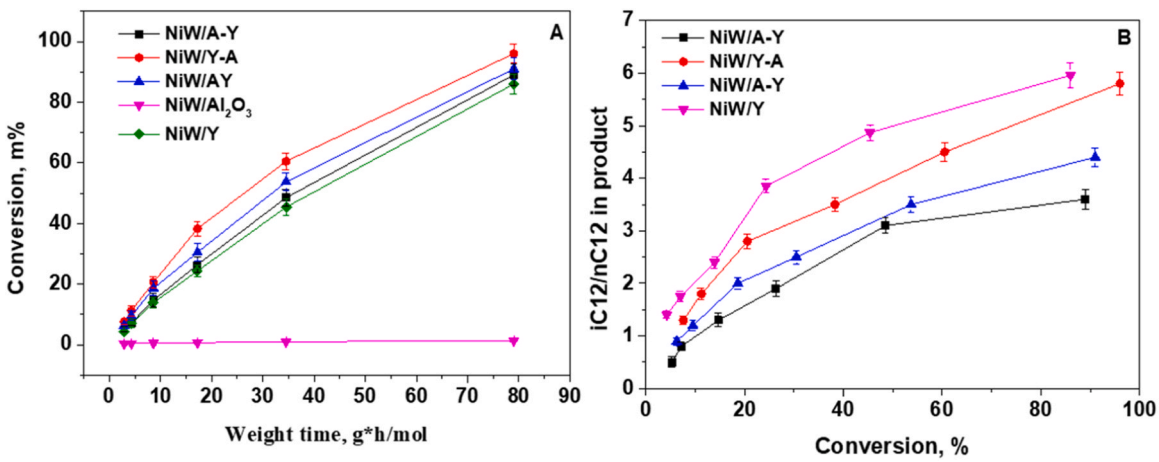

Fig. 11. the hydrocracking conversions of n-dodecane over different catalysts (A); the ratios of iC12 and nC12 in liquid product (B).

The ratios of iC12 and nC12 in the liquid product for all the catalysts are shown in Fig. 11B. It shows an order of NiW/A-Y < NiW/AY < NiW/Y-A < NiW/Y. For the NiW/Y-A and NiW/Y catalysts, there are more active metal loading on the Y zeolite. Therefore, their distances between the hydrogenation center and cracking center are closer than those for the NiW/AY and NiW/A-Y catalysts. Meanwhile, the active metals are loaded on Al_2O_3 and then mixed with Y zeolite for the NiW/A-Y catalyst, indicating that its distance between the hydrogenation center and cracking center is the farthest. Interestingly, the ratio of iC12 and nC12 in the product follows a reverse trend as the distance between the hydrogenation center and cracking center of the NiW catalysts. In addition, the ratios of iC and nC in the liquid product for all the catalysts are also shown in Fig. S8. It follows the order of NiW/A-Y < NiW/AY < NiW/Y-A < NiW/Y, which is similar with the ratio of iC12 and nC12. Therefore, it can be deduced that a closer distance between the hydrogenation center and cracking center of the NiW catalyst will lead to a higher ratio of isomerized product as hydrocracking n-dodecane.

However, Zečević reported that Pt/Al_2O_3 mixed with Y zeolite shows higher selectivity for iso-alkanes than Pt/Y-A with far distance between acid and metal sites. The author ascribed the reason to a nanoscale intimacy between the hydrogenation and cracking center for the Pt/Al_2O_3-Y catalyst [13]. The difference between the two results should be related to different distances between acid and metal sites and the abilities of active metals to dissociate hydrogen. On the one hand, the ability of Pt to dissociate hydrogen is much better than that of NiW metals, on the other hand, the distance between acid and metal sites is longer for NiW/A-Y catalyst than that of the Pt/Al_2O_3-Y catalyst. According to Scheme 2, the iso-alkanes are formed by the hydrogenation of iso-alkene intermediates. For the NiW/A-Y catalyst, the lower concentration of active hydrogen and longer distance between acid and metal sites lead to difficulties of saturating iso-alkene intermediates and then forming iso-alkanes. Therefore, the isomerization selectivity of hydrocracking n-dodecane for NiW/A-Y catalyst is relatively low.

The liquid yields of the n-dodecane hydrocracking reaction over different catalysts are shown in Fig. 12. It can be clearly seen that the liquid yield of the n-dodecane hydrocracking reaction over the NiW/A-Y catalyst is lower than that of the other catalysts under the same reaction

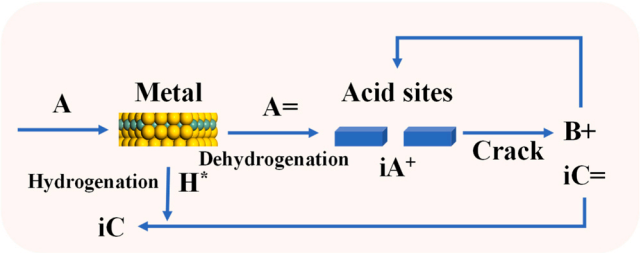

Scheme 2. the principle of hydrocracking reactions over a bifunctional catalyst. n-alkane (A) is dehydrogenated on active metals, producing alkene intermediates (A=). The A= diffuse to acid sites, on which isomerization and cracking reactions undergo, which will further produce (B+) and (iC=) cracking intermediates. Alkene intermediates (iC=) will be hydrogenated by active hydrogen to isomerized alkanes (iC).

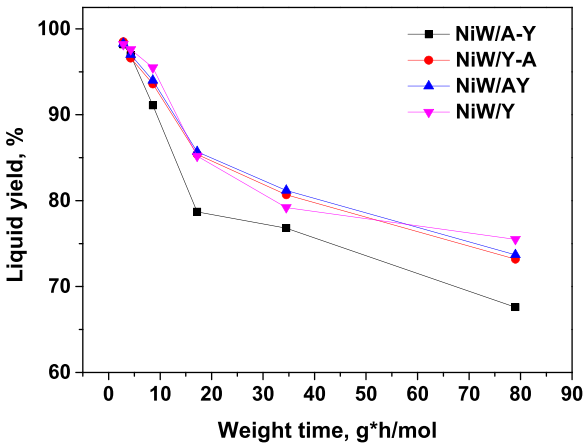

Fig. 12. the liquid yields of n-dodecane hydrocracking reaction over different catalysts.

conditions. Therefore, it can also be deduced that a large distance between the hydrocracking center and hydrogenation center will decrease the liquid yield. Noticeably, the NiW/A-Y catalyst presents the lowest hydrocracking activity and but lowest liquid yield. This phenomenon can be explained from Scheme 2. The alkene intermediates (A=) can hardly diffuse to acid sites and produce (B+) for further cracking over NiW/A-Y catalyst, which will lead to a low hydrocracking activity. As the B+ is formed over acid sites, the active hydrogen can hardly reach and saturate the (iC=) cracking intermediates, which will cause excessive cracking and lower liquid yield.

The n-dodecane hydrocracking performances evaluated at various temperatures over different catalysts are shown in Fig. 13A. The pressure, weight time and volume ratio of hydrogen and oil are fixed at 4 MPa, 2.87 g*h/mol and 100, respectively. The corresponding Arrhenius plots (*lnk* vs. 1/*T*) of different catalysts are shown in Fig. 13B. The active energy (*Ea*) can be obtained based on the slopes of the linear Arrhenius plots. Meanwhile, the kinetic constants and TOF for the n-dodecane hydrocracking reaction over different catalysts are calculated, and the results are shown in Table 6. The total reaction rate constant *k* follows the order of NiW/Y (4.65 *10^{-6} mol g^{-1} s^{-1}) < NiW/A-Y (4.81 *10^{-6} mol g^{-1} s^{-1}) < NiW/AY (6.49 *10^{-6} mol g^{-1} s^{-1}) < NiW/Y-A (7.70 *10^{-6} mol g^{-1} s^{-1}). The NiW/Y and NiW/Y-A catalysts also show relatively higher ratios of isomerization *k* constant (k_{iso}) and cracking to normal product *k* constant (k_d) than the other two catalysts. The activation energies (*Ea*) follow the order of NiW/Y-A (4.68 kJ/mol) < NiW/AY (5.31 kJ/mol) < NiW/A-Y (6.92 kJ/mol) < NiW/Y (7.71 kJ/mol). According to the reported literature, a lower *Ea* value indicates a higher

Table 6
kinetic constants and TOF of n-dodecane hydrocracking reaction, as the conversions are controlled at about 20%.

Catalyst	*k* (10^{-6} mol g^{-1} s^{-1})	k_d[a] (10^{-6} mol g^{-1} s^{-1})	k_{iso}[b] (10^{-6} mol g^{-1} s^{-1})	*Ea* (kJ/mol)	TOF[a] (h^{-1})
NiW/A-Y	4.81	0.93	3.88	6.92	146.44
NiW/Y-A	7.70	0.98	6.72	4.68	252.29
NiW/AY	6.49	1.04	5.45	5.31	178.98
NiW/Y	4.65	0.55	4.10	7.71	-

[a] : k_d= *k* * proportion of n-Cn in the product.
[b] : k_{iso}=k-k_d.

conversion [56]. In addition, the TOF values of different catalysts follow the order of NiW/A-Y (146.44 h^{-1}) < NiW/AY (178.98 h^{-1}) < NiW/Y-A (252.29 h^{-1}). Hence, the kinetic study confirms that the NiW/Y-A catalyst and NiW/Y catalyst present the highest activity and worst n-dodecane hydrocracking performances, respectively. The NiW/Y-A catalyst and NiW/Y catalyst also present higher selectivities of iso-alkanes than NiW/A-Y and NiW/AY catalysts as hydrocracking n-dodecane, which is consistent with the results from Fig. 11.

The influence of pressure on n-dedocane hydrocracking performance is investigated over the NiW/Y-A catalyst. The H_2/oil ratio is fixed at 100. The reaction temperature was fixed at 320 °C. The pressures are adjusted from 2 to 8 MPa, and the weight times are adjusted from 2.9 to 79 g*h/mol. The hydrocracking results are shown in Fig. S9. It can be seen from Fig. S9A that the n-dodecane hydrocracking activity increases little with increasing pressure. However, the pressure plays an important role in the selectivity of the isomerization reaction. As shown in Fig. S9B, a low pressure will lead to a high selectivity of isomerization; this is related to the fact that a high hydrogen pressure decreases the formation of iso-alkene intermediates and the further cracking reaction.

The n-dodecane hydrocracking behaviors of the NiW/Y-A catalyst and the referred catalysts with the same amounts of zeolites and metals were evaluated at the same conditions of a pressure of 4 MPa, H_2/oil ratio of 100, weight time of 79 g*h/mol and temperature of 320 °C. The Ref 1. and Ref 2. catalysts were prepared according to the literatures, respectively [57,58]. The NiW/HY-Al_2O_3 catalyst in Ref 1. is composed of 5.3 wt% NiO, 19.0 wt% and 37.85 wt% HY. The catalyst in Ref 2. is composed of HY (Y-1) zeolite. The above industrial HY zeolites are prepared by Dalian Research Institute of Petroleum and Petrochemicals, SINOPEC. The corresponding n-dodecane hydrocracking results are shown in Fig. 14. The results show that the hydrocracking activity and selectivity of isomerization for NiW/Y-A are higher than those of catalysts from the literature and industry.

For the NiW/Y-A catalyst, the yields of paraffins in the liquid product

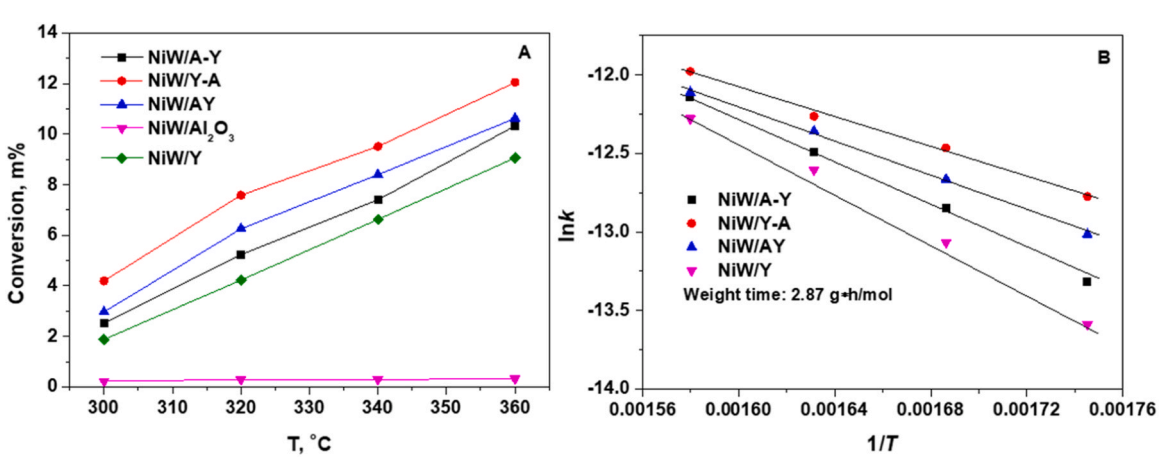

Fig. 13. Arrhenius plots of different catalysts.

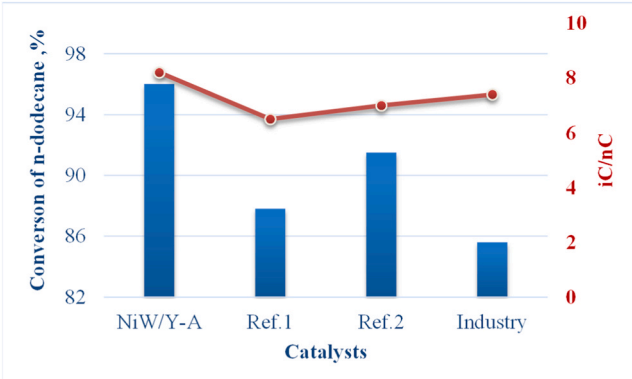

Fig. 14. the comparison of n-dodecane hydrocracking behaviors between NiW/Y-A catalyst and referred catalysts. (The blue bar is corresponding to left Y of conversion of n-dodecane; the red line is corresponding to right Y axis of iC/nC).

at various hydrocracking conversions are shown in Fig. 15A. The reaction pressure is fixed at 4 MPa, and the H_2/oil ratio is fixed at 100. Under the same conditions, the yields of the product follow the order of C11 < C10 < C9 < C5 < C8 < C6 < C7. Paraffins with carbon numbers from 6 to 8 are the most likely product. The paraffins with carbon numbers from 9 to 11 are lower. It can be deduced that the breaks of methyl, ethyl and propyl groups from n-dodecane are difficult to occur. In addition, the product yields and conversion rates are almost linearly correlated. The conversion factor (C*f*) was calculated by dividing the change in yield (Δy) by the change in conversion (Δc from 4% to 19.8%). The C*f* values of paraffins with different carbon numbers are shown in Fig. 15B. The C*f* values of C6, C7 and C8 are higher than those of other paraffins, confirming that the formation of C6, C7, and C8 is more preferable to produce than to further break under a certain range of conversions.

The cracking of paraffins follows the carbocation and β-cracking mechanism. In the liquid product, the proportions of isomerized paraffins with carbon numbers from 4 to 9 are higher than those of normal paraffins. Combined with the product distribution from Fig. 15A, the main reaction steps of n-dodecane hydrocracking are shown in Scheme 3. The n-dodecane initially adsorbs on the active metals and dehydrogenates to olefins. The medium reactant of olefins can accept the hydrogen proton from zeolite and be protonated and isomerized. After β-cracking and hydrogenation reactions, light paraffins are formed. Among the protonation and isomerization steps, protonated i-C6, i-C5 and i-C4 are most likely to be formed and peeled off. The remaining part is mainly isomerized paraffins, but the heterogeneous location is uncertain and random.

3.3. Stabilities of catalysts

Raman spectra of the evaluated NiW/A-Y, NiW/Y-A and NiW/AY catalysts are shown in Fig. 16. All the Raman spectra present two obvious bands at approximately 1370 cm^{-1} (D-band) and 16000 cm^{-1} (G-band). The D-band indicates edges, disorder and defects in the hexagonal graphitic layers, and the G-band results from the vibration of sp2-carbon atoms in a 2D hexagonal lattice [59]. The intensity ratio of the D-band and G-band in Raman spectra is considered indicative of defects in carbon materials [60]. The intensity ratios of the D-band and G-band for the NiW/A-Y, NiW/Y-A and NiW/AY catalysts are 0.64, 0.62 and 0.56, respectively. The NiW/A-Y catalyst shows a higher intensity ratio of the D-band and G-band, suggesting that the carbon layers in the NiW/A-Y catalyst possess more defects.

TG-DTA measurements were applied to obtain the amounts of carbon deposition over different catalysts. The TGA results are shown in Fig. 17, and the DTA spectra are shown in Fig. S10. There are three forms of carbon: amorphous carbon (<250 °C), atomic carbon (250–600 °C) and graphitic carbon (>600 °C) [61]. The total mass losses from 30° to 900°C for NiW/A-Y, NiW/Y-A and NiW/AY catalysts are 29.4%, 20.2% and 18.8%, respectively. The carbon deposition over the NiW/A-Y catalyst is more severe than that over the NiW/Y-A and NiW/AY catalysts, indicating that a far distance between active metals and acid sites will lead to more carbon deposition. According to the reaction scheme of n-dodecane, as the protonated and isomerized intermediate reactant is cracked over Y zeolite, olefins are formed and must be quickly hydrosaturated. Otherwise, the olefins are aggregated over the acid sites. Therefore, loading certain amounts of active metals over acidic support for cracking, which decreases the distance between hydrogenation centers and cracking centers, can decrease the amounts of deposited carbon. In addition, the NiW/Y-A and NiW/AY catalysts present similar amounts of deposited carbon.

The n-dodecane hydrocracking performances of different catalysts over a long period of 92 h are evaluated, and the results are concluded in Fig. S11A. After running for 92 h, the conversions of n-dodecane for the NiW/A-Y catalyst decreased sharply from 26.4% to 20%. The conversion of hydrocracking n-dodecane for the NiW/Y-A and NiW/AY catalysts decreased by 0.9% and 1.2%, respectively. Hence, the stabilities of the NiW/Y-A and NiW/A- catalysts are better than that of the NiW/A-Y catalyst. The lower stability of the NiW/A-Y catalyst is correlated to its greater carbon deposition, which covers the hydrogenation and cracking center. In addition, the influence of pressure on the stability of the NiW/Y-A catalyst was investigated, and the results are shown in

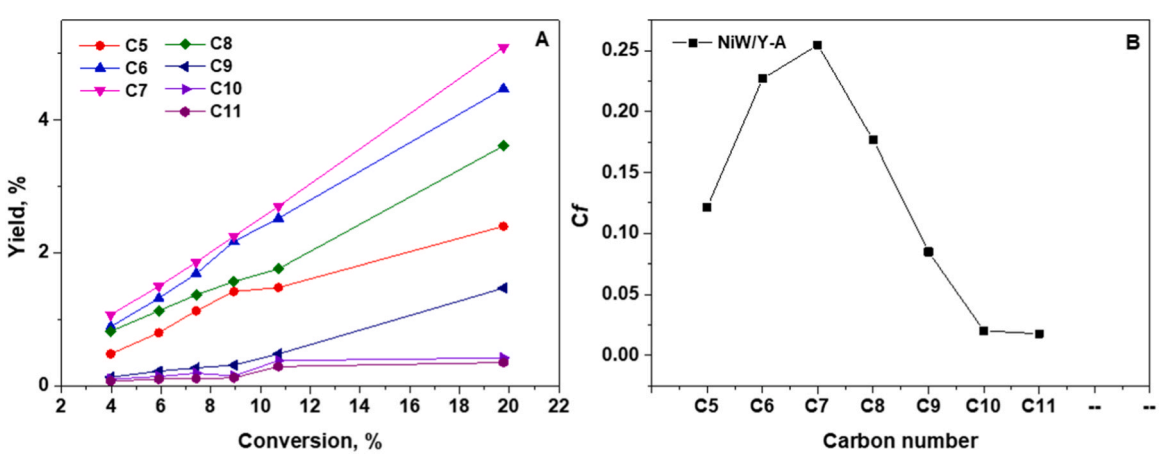

Fig. 15. (A) the relationship between conversions and yields of paraffins with different carbon numbers; (B) conversion factors (C*f*) of paraffins with different carbon numbers for NiW/Y-A catalyst.

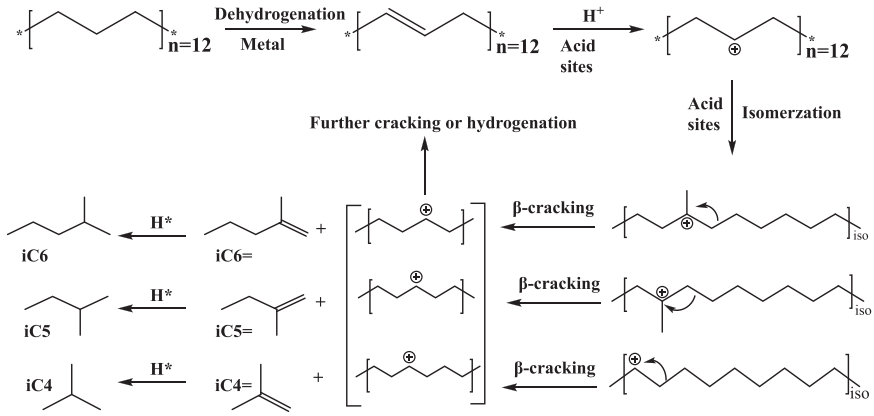

Scheme 3. the main reaction steps of n-dodecane hydrocracking reaction.

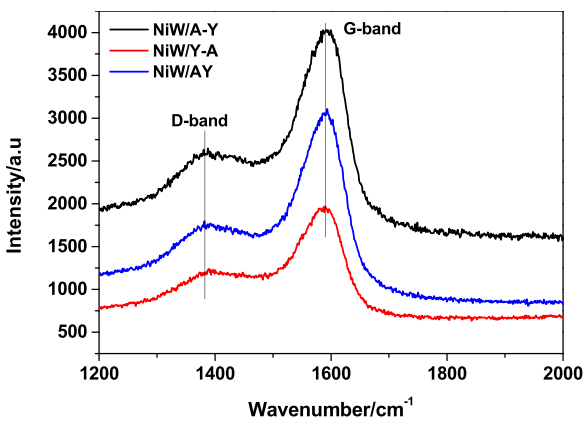

Fig. 16. Raman spectra of different evaluated catalysts.

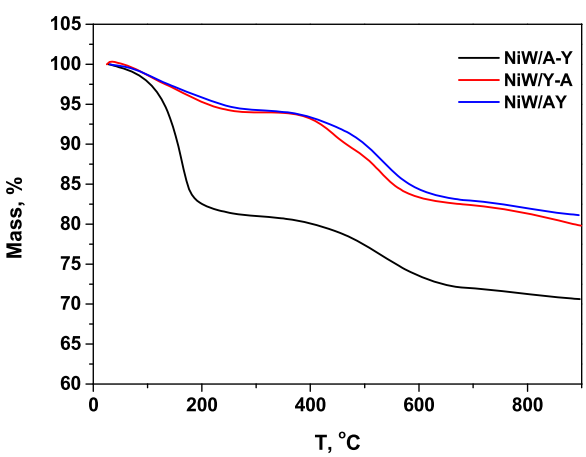

Fig. 17. TG-DTA patterns of different evaluated catalysts.

Fig. S11B. As the pressure is higher than 4 MPa, the deactivation rate of the NiW/Y-A catalyst is relatively low. However, as the pressure reached 2 MPa, the stability of the NiW/Y-A catalyst became too poor. Therefore, pressure plays an important role in the stability of hydrocracking catalysts.

4. Conclusion

In our study, a series of hydrocracking catalysts containing Y zeolite with micropores and mesoporous Al_2O_3 were prepared and compared to investigate the influences of the distance between the hydrogenation center and cracking center and diffusivities on the hydrocracking performance. The results demonstrated that the dispersion degree of active metals followed the order of NiW/Y-A < NiW/A-Y < NiW/AY. The ZLC results revealed that introducing an appropriate amount of mesoporous Al_2O_3 into the micro zeolite could significantly enhance the diffusivity. Meanwhile, the oxide and sulfide NiW/Y-A catalysts exhibited the best diffusivity due to the introduction of pure mesoporous Al_2O_3. The oxide NiW/Y-A catalyst with the lowest *K'* value and the best desorption ability can be related to its weakest acidity, largest particle size and worst dispersion of active metals, which will lead to the weakest adsorption strength between adsorbate and adsorbent among the combined catalysts. The XPS and HRTEM results showed that the proportions and dispersion degree of active WS_2 phases of sulfide catalysts followed the order of NiW/Y-A < NiW/A-Y < NiW/AY.

The n-dodecane hydrocracking evaluation results showed that the NiW/Y-A catalyst with low pore size and pore volume, poor dispersion of active metals and weak acidities shows the highest conversion of cracking n-dodecane, which can be attributed to the fact that the NiW/Y-A catalyst possesses the best diffusivity. Meanwhile, the NiW/Y-A catalyst and NiW/Y catalyst also present higher selectivities of isoalkanes than the NiW/A-Y and NiW/AY catalysts toward n-dodecane hydrocracking, demonstrating that a closer distance between the hydrogenation center and cracking center of the bifunctional catalyst would lead to a higher ratio of iC12 and nC12 in the product. Noticeably, the liquid yield of n-dodecane hydrocracking for NiW/A-Y is lower than that of other catalysts due to the far distance between the hydrogenation center and cracking center.

Finally, the stabilities of different hydrocracking catalysts were investigated through long-term evaluation. This result showed that a closer distance between the hydrogenation center and cracking center of the bifunctional catalyst could decrease the amount of deposited carbon and improve the hydrocracking stability.

CRediT authorship contribution statement

Z. Cao: Investigation, Formal analysis, Writing – original draft. **S. Ding:** Investigation, Formal analysis. **R. Guo:** Investigation, Conceptualization. **Z. Chen:** Investigation, Formal analysis. **J. Yu:** Formal analysis. **Z. Wu:** Conceptualization, Supervision. **D. Gao:** Project administration, Funding acquisition. **A. Duan:** Conceptualization, Supervision. **H. Liu:** Formal analysis. **X. Zhang:** Writing – review & editing, Funding acquisition, Formal analysis.

Declaration of Competing Interest

The authors declare no competing financial interest.

Data Availability

Data will be made available on request.

Acknowledgements

This work was supported by the National Key R&D Program of China (2018YFA0209404, 2022YFA1504404), the National Natural Science Foundation of China (No. 21878330, 22278174), the CNPC Key Research Project (2016E-0707), the Shandong Excellent Young Scientists Fund Program (Overseas, 2022HWYQ-082).

Appendix A. Supporting information

Supplementary data associated with this article can be found in the online version at doi:10.1016/j.apcatb.2023.123536.

References

[1] B.C. Vance, P.A. Kots, C. Wang, Z.R. Hinton, C.M. Quinn, T.H. Epps, L.T.J. Korley, D.G. Vlachos, Appl. Catal. B 299 (2021), 120483.
[2] M. Grilc, L.J. B. Levec, Appl. Catal. B 150–151 (2014) 275–287.
[3] Y. Kim, K. Cho, Y. Lee, J. Catal. 351 (2017) 67–78.
[4] L. Qi, C. Peng, Z. Cheng, Z. Zhou, Chem. Eng. Sci. 263 (2022), 118121.
[5] Z. Cao, X. Zhang, C. Xu, X. Huang, Z. Wu, C. Peng, A. Duan, J. Energy Chem. 52 (2021) 41–50.
[6] S. Maheshwari, E. Jordan, S. Kumar, F.S. Bates, R.L. Penn, D.F. Shantz, M. Tsapatsis, J. Am. Chem. Soc. 130 (2008) 1507–1516.
[7] W. Fan, M.A. Snyder, S. Kumar, P.S. Lee, W.C. Yoo, A.V. Mccormick, R.L. Penn, A. Stein, M. Tsapatsis, Nat. Mater. 7 (2008) 984–991.
[8] S. Maheshwari, C. Martínez, M.T. Portilla, F.J. Llopis, A. Corma, M. Tsapatsis, J. Catal. 272 (2010) 298–308.
[9] J. Karger, D.M. Ruthven, D.N. Theodorou, Medium-Pore (Ten-Ring) Zeolites. Diffusion in Nanoporous Materials, Wiley-VCH Verlag GmbH & Co. KGaA: Weinheim, Germany, 2012, pp. 653–728.
[10] D. Liu, A. Bhan, M. Tsapatsis, S.A. Hashimi, ACS Catal. 1 (2011) 7–17.
[11] K.P. de Jong, J. Zecevic, H. Friedrich, P.E. de Jongh, M. Bulut, S. van Donk, R. Kenmogne, A. Finiels, V. Hulea, F. Fajula, Angew. Chem., Int. Ed. 49 (2010) 10074–10078.
[12] P.B. Weisz, Adv. Catal. 13 (1962) 137–190.
[13] J. Zecevic, G. Vanbutsele, K.D. Jong, J.A. Martens, Nature 528 (2015) 245–248.
[14] E. Gutierrez-Acebo, C. Leroux, C. Chizallet, Y. Schuurman, C. Bouchy, ACS Catal. 8 (2018) 6035–6046.
[15] J. Oenema, J. Harmel, R.P. Vélez, M.J. Meijerink, W. Eijsvogel, A. Poursaeidesfahani, T.J.H. Vlugt, J. Zečević, K., P. de Jong, ACS Catal. 10 (2020) 14245–14257.
[16] J. Sun, C. Mu, D. Guo, Y. Zhao, S. Wang, X. Ma, ACS Catal. 12 (2022) 4092–4102.
[17] W. Zhou, W. Qiang, Y. Zhou, M. Liu, S. Ding, Y. Qi, Appl. Catal. B 238 (2018) 212–224.
[18] A. Kostyniuk, D. Bajec, B. Likozar, Appl. Catal. A 612 (2021), 118004.
[19] A. Kostyniuk, D. Bajec, B. Likozar, Renew. Energy 167 (2021) 409–424.
[20] Z. Cao, Z. Wu, J. Mei, R. Zeng, S. Hou, S. Peng, A. Duan, X. Zhang, ACS Sustain. Chem. Eng. 9 (2021) 12415–12426.
[21] O. Ben Moussa, L. Tinat, X. Jin, W. Baaziz, O. Durupthy, C. Sayag, J. Blanchard, ACS Catal. 8 (2018) 6071–6078.
[22] J.E. Samad, J. Blanchard, C. Sayag, C. Louis, J.R. Regalbuto, J. Catal. 342 (2016) 213–225.
[23] N. Batalha, L. Pinard, Y. Pouilloux, M. Guisnet, Catal. Lett. 143 (2013) 587–591.
[24] Y. Sun, R. Prins, J. Catal. 267 (2009) 193–201.
[25] L. Karakonstantis, H. Matralis, C. Kordulis, A. Lycourghiotis, J. Catal. 162 (1996) 306–319.
[26] S. Shan, Y. Pei, H. Wei, S. Gang, X. Bao, J. Catal. 330 (2015) 288–301.
[27] J.N. Diaz de León, A.L. Castaeda-García, C.E. Soto-Arteaga, G. Torres-Otaez, S. Fuentes-Moyado, Catal. Today 377 (2021) 59–68.
[28] D.G. Barnton, M. Shtein, R.D. Wilson, S.L. Soled, E. Iglesia, J. Phys. Chem. B 103 (1999) 630–640.
[29] Z. Cao, A. Duan, Z. Zhao, J. Li, Y. Wei, G. Jiang, J. Liu, J. Mater. Chem. A 2 (2014) 19738–19749.
[30] R. Weber, J. Catal. 151 (1995) 470–474.
[31] J.B. Peri, J. Catal. 86 (1984) 84–94.
[32] G. Poncelet, M.A. Centeno, R. Molina, Appl. Catal. A 288 (2005) 232–242.
[33] L. Daza, B. Pawelec, J.A. Anderson, J. Fierro, Appl. Catal. A 87 (1992) 145–156.
[34] S. Ewald, M. Kolbeck, T. Kratky, M. Wolf, O. Hinrichsen, Appl. Catal., A 570 (2019) 376–386.
[35] Z. Cao, X. Zhang, R. Guo, S. Ding, J. Mei, X. Wang, P. Zheng, J. Fan, C. Xu, A. Duan, ACS Catal. 10 (2020) 12342–12353.
[36] J.N. Díazde León, M. Picquart, M. Villarroel, M. Vrinat, F.J. Gil Llambias, F. Murrieta, J.A. de los Reyes, *J. Mol. Catal. A* 323 (2010) 1–6.
[37] R. Huirache-Acuña, B. Pawelec, E. Rivera-Munoz, R. Nava, J. Espino, J.L.G. Fierro, Appl. Catal. B 92 (2009) 168–184.
[38] Anon.
[39] X. Yang, W. Dai, R. Gao, K. Fan, J. Catal. 249 (2007) 278–288.
[40] J. Xu, Y. Guo, T. Huang, Y. Fan, Appl. Catal. B 244 (2019) 385–395.
[41] J. Xu, Y. Guo, T. Huang, Y. Fan, Appl. Catal. B 244 (2019) 385–395.
[42] Y. Yoshimura, T. Sato, H. Shimada, N. Matsubayashi, M. Imamura, A. Nishijima, M. Higo, S. Yoshitomi, Catal. Today 29 (1996) 221–228.
[43] M. Eic, D.M. Ruthven, Zeolites 8 (1988) 40–45.
[44] L. Hu, Z. Chen, W. Sun, T. Cheng, Y. Wei, C. Xu, S. Zhao, *Ind. Eng. Chem. Res.* 59 (2020) 8426–8435.
[45] L. Qiu, G. Xu, *Appl. Surf. Sci.* 256 (2010) 3413–3417.
[46] P. Guo, X. Wang, H. Guo, Appl. Catal. B 90 (2009) 677–687.
[47] Y. Yeh, C. Rzepa, S. Rangarajan, R. Gorte, Microporus Mesoporous Mat. 284 (2019) 336–342.
[48] J. Wang, S. Ding, S. Peng, Z. Yang, Y. Du, RSC Adv. 12 (2022) 19537–19547.
[49] A. Pashigreva, E. Kondratieva, R. Bermejo-Deval, O. Gutiérrez, J. Lercher, J. Catal. 345 (2017) 308–318.
[50] D. Zhang, X. Cen, H. Wen, H. Wang, J. Deng, R. Tang, C. Shu, J. Loss Prev. Proc. 84 (2023), 105127.
[51] Q. Jia, D. Liu, Y. Cai, Y. Yao, Y. Lu, Y. Zhou, Chem. Eng. J. 452 (2023), 139511.
[52] L.A. Zavala-Sanchez, X. Portier, F. Maugé, L. Oliviero, ACS Catal. 10 (2020) 6568–6578.
[53] E. Dominguez Garcia, J. Chen, E. Oliviero, L. Oliviero, F. Maugé, *Appl. Catal. B: Environ.* 260 (2020) 117975–117987.
[54] A. Travert, C. Dujardin, F. Maugé, E. Veilly, S. Cristol, J.F. Paul, E. Payen, J. Phys. Chem. B 110 (2006) 1261–1270.
[55] B. Pawelec, R. Mariscal, J. Fierro, A. Greenwood, P.T. Vasudevan, Appl. Catal. A 206 (2001) 295–307.
[56] M.L. Vrinat, Appl. Catal. 6 (1983) 137–158.
[57] C. Peng, Z. Zhou, Z. Cheng, X. Fang, Energ. Fuel 33 (2019) 1090–1097.
[58] Y. Guo, H. Jia, J. Qi, B. Fan, B. Qin, J. Ma, Y. Du, R. Li, *Catal. Commun.* 177 (2023), 106655.
[59] G. Huang, T. Chen, W. Chen, Z. Wang, K. Chang, L. Ma, F. Huang, D. Chen, J.Y. Lee, Small 9 (2013) 3693–3703.
[60] Z. Wang, T. Chen, W. Chen, K. Chang, L. Ma, G. Huang, D. Chen, J.Y. Lee, J. Mater. Chem. A 1 (2013) 2202–2210.
[61] A. Effendi, Z. Zhang, K. Hellgardt, K. Honda, T. Yoshida, Catal. Today 77 (2002) 181–189.